Nanoscale

Accepted Manuscript

This article can be cited before page numbers have been issued, to do this please use: D. Kim, D. Ha, Q. Zhou, A. K. Thokchom, J. Lim, J. Lee and T. Kim, *Nanoscale*, 2017, DOI: 10.1039/C7NR02354E.

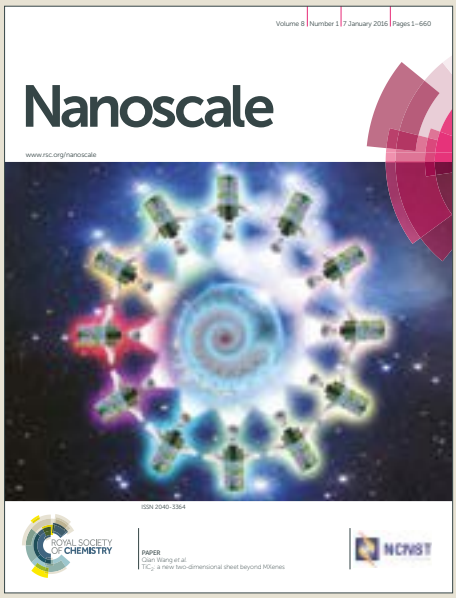

ROYAL SOCIETY OF CHEMISTRY

rsc.li/nanoscale

Cracking-assisted Micro-/Nanofluidic Fabrication Platform for Silver Nanobelt Arrays and Nanosensors

Dong-Joo Kim[1,2], Dogyeong Ha[1], Qitao Zhou[1], Ashish Kumar Thokchom[1], Jiwon Lim[1], Jongwan Lee[1], and Taesung Kim[1,3*]

[1]Department of Mechanical Engineering, Ulsan National Institute of Science and Technology (UNIST), 50 UNIST-gil, Ulsan 44919, Republic of Korea.

[2]Department of Biomedical Engineering, Yale University, New Haven, CT 06520, USA.

[3]Department of Biomedical Engineering, Ulsan National Institute of Science and Technology (UNIST), 50 UNIST-gil, Ulsan 44919, Republic of Korea.

[*]Corresponding author
Taesung Kim
Department of Mechanical Engineering
Ulsan National Institute of Science and Technology (UNIST)
50 UNIST-gil, Ulsan 44919, Republic of Korea
E-mail: tskim@unist.ac.kr

Keywords: crack-photolithography, micro-/nanofluidic channels, silver nanobelt arrays, flexible substrate, chemical sensor

View Article Online
DOI: 10.1039/C7NR02354E

Abstract

Nanowires (NWs) with high surface-to-volume ratio are advantageous for bio- or chemical sensor applications with high sensitivity, high selectivity, rapid response, and low power consumption. However, NWs are typically fabricated by combining several nanofabrication and even microfabrication processes, resulting in drawbacks such as high fabrication cost, extensive labor, and long processing time. Here, we show a novel NW fabrication platform based on "crack-photolithography" to produce a micro-/nanofluidic channel network. Solutions were loaded along the microchannel, while chemical synthesis was performed in the nanoslit-like nanochannels for fabricating silver nanobelts (AgNBs). In addition, the NW/NB fabrication platform not only made it possible to produce AgNBs in a repeatable, high-throughput, and low-cost manner but also allowed the simultaneous synthesis and alignment of AgNBs on a chip, eliminating the need for special micro- and/or nanofabrication equipment and dramatically reducing the processing time, labor, and cost. Finally, we demonstrated that the AgNBs can be used as chemical sensors, either as prepared or when integrated in a flexible substrate, to detect target analytes such as hydrogen peroxide.

View Article Online
DOI: 10.1039/C7NR02354E

1. Introduction

Nanowires (NWs) play a crucial role in electronics,[1] photonics,[2] and bio/chemical sensors[3] because of several advantages such as low power consumption, molecular level characteristic length, and high surface-to-volume ratio.[4] Current NW fabrication and manipulation methods can be categorized into two types: bottom-up and top-down. In the bottom-up methods, NW arrays are first prepared by using several techniques,[5-7] followed by manipulation of the prepared NWs on a circuit plane under single, multiple, and random manners.[2, 8-10] However, these methods require special tools for synthesizing and manipulating the NWs, and precise control of the NW position at the desired location is difficult.[11] In contrast, in top-down methods, nanoscale patterns are first generated at the desired position, and then, NWs are fabricated by deposition, growth, and etching processes.[1, 12-15] Although these technologies can generate NWs at the exact position at a high resolution, there are limitations in terms of the fabrication throughput, and the cost and time required for obtaining large-scale nanopatterns.[16] To simultaneously fabricate and manipulate NWs using conventional lithographic technology, edge lithography and meniscus-mask lithography have been proposed.[17, 18] However, multiple deposition and etching processes are required to fabricate NWs using these lithography methods. Consequently, these processes still require expensive facilities for the metal deposition and etching.

Recently, some unconventional NW fabrication methods were reported; these belong to the category of top-down methods and mainly rely on material failure.[19] For example, Jebril et al. created a nanoscale crack pattern on bow-tie-like micropatterns in a photoresist film by inducing tensile stress via a thermal cycle, and fabricated zinc oxide NWs via sputtering and applied it to the detection of gaseous oxygen.[20] This cracking technique produced multiscale micro-/nanopatterns on the same surface, and the NWs were easily integrated and connected to microelectrodes over a large-scale wafer. However, precise modulation of geometrical dimensions and suppression of unwanted crack remain a challenge. Here, we report a novel

View Article Online
DOI: 10.1039/C7NR02354E

NW fabrication platform to overcome the drawbacks associated with unconventional NW fabrication techniques. The new fabrication platform enables the simultaneous synthesis and manipulation of a NW array. This is made possible by combining a micro-/nanofluidic channel network, which is repeatedly and easily produced using "crack-photolithography" – a process that has been well established in our previous work – and the Tollens' reaction, which is widely used for the chemical deposition and mass production of Ag coatings on various substrates, so that a silver nanobelt (AgNB) array is fabricated along the nanoslit-shaped nanofluidic channels. This work shows that the fabrication platform not only provides an unprecedented, simple, and innovative approach for producing a NB array on various substrates but also allows for the transfer of such NB arrays and their integration into polydimethylsiloxane (PDMS)-based micro-/nanofluidic devices. Lastly, we test the fabricated device in the detection of H_2O_2 because of the importance of this chemical in various day-to-day activities.[3]

2. Experimental

2.1. Reagents and materials

A negative photoresist of SU-8 (SU-8 2010, MicroChem, Westborough, USA) was used for crack-photolithography, while another negative photoresist (AZ5214, Clariant Corporation, Somerville, NJ) was used for electrode patterning. Regular polydimethylsiloxane (PDMS, Sylgard 184 silicone elastomer kit, Dow Corning, Midland, MI, USA) was purchased for soft-lithography. Hard-PDMS (h-PDMS) consisting of VDT-731 (3.4 g, JSI Silicone, Seongnam, Korea), a platinum catalyst (18 μL, JSI silicone), and 2,4,6,8-tetramethyltetravinylcyclotetrasiloxane (4 μL, Sigma-Aldrich) was also prepared and used.[21] A polyurethane acrylate (PUA) solution, MINS-311RM, and a polyethylene terephthalate (PET) film were used for replication of the SU-8 master (all from Minuta Tech., Osan, Gyeonggi, Korea). Silver nitrate ($AgNO_3$) and D-glucose were purchased from Sigma Aldrich

View Article Online
DOI: 10.1039/C7NR02354E

(St. Louis, USA). Potassium hydroxide (KOH) and ammonium hydroxide (NH_4OH) were purchased from Dong Yang Chemical Co., Ltd. (Yeongam, Korea). All reagents were of analytical grade and used without further purification.

2.2. Crack-photolithography for micro-/nanopatterns

"Crack-photolithography" was conducted using the same fabrication process described in our previous report to obtain hybrid-scale micro-/nanopatterns on negative photoresist films (Figure S1).[22, 23] In this study, 10-μm-thick SU-8 films were spin-coated on a 6-inch silicon wafer and subsequently soft baked on a hot plate at 95 °C for 3 min. The SU-8 film was then exposed to ultraviolet (UV) light through the first photomask, which had micropatterns including crack initiation and termination patterns, using a mask aligner (MA6, Suss MicroTec Ag, Schleissheimer, Germany) without any UV filters to generate the cross-linking gradient in the direction of the thickness.[24] The UV exposure energy (120 mJ/cm^2) was reduced to the minimum dose (70 mJ/cm^2) that did not cause delamination of the SU-8 films from the substrate during the development process. The development process was carried out by immersing the SU-8 films in the developer so that isotropic tensile stress was induced on the microscale patterns via the swelling effect of the films. Thus, cracks propagated from the notch structures to flat and/or circular structures, as previously reported.[23] After the first post-exposure baking (PEB) on a hot plate at 95 °C for 3 min, the SU-8 films were developed for an additional 1 min to obtain micropatterns. The development process was carried out without agitation, which minimized unnecessary stress. Next, the SU-8 films were exposed to UV radiation at 90 mJ/cm^2 under the second photomask for complete suppression of unwanted cracks, and then subjected to the second PEB under the same baking conditions as the first one. Lastly, the second development process was performed for 30 min to generate crack nanopatterns only within the single UV-exposed area. In this paper, this fabrication process is referred to as "standard crack-photolithography".

2.3. Fabrication of micro-/nanofluidic devices via soft-lithography

View Article Online
DOI: 10.1039/C7NR02354E

Micro-/nanopatterns of SU-8 files were replicated using a PUA solution and a PET film. Before pouring a PUA solution on an SU-8 master mold, a custom-made nitrogen chamber was used to remove oxygen gas, which can inhibit photocuring of the PUA solution. Oxygen-free conditions can ensure perfect replication of the micro-/nanopatterns on an SU-8 mold without significant volume reduction during the phase change. Then, the UV-cured PUA on the PET film was peeled off from the SU-8 mold, and, subsequently, the PUA pattern was used as another mold for PDMS. To prevent roof collapse, hard-PDMS (h-PDMS) was spin-coated at 1,000 rpm on the PUA mold and cured in a hot oven at 75 °C for 30 min. Then, the PDMS mortar was poured onto the h-PDMS-coated PUA mold, and cured in a hot oven again at 75 °C for 4 h. Before bonding the PDMS device with the silicon or glass substrate for AgNB synthesis, the device was soaked in deionized water and kept overnight at 4 °C to circumvent the nanochannel evaporation effect.[25]

2.4. Synthesis of AgNBs

The Tollens' reaction enables a simple, inexpensive, and eco-friendly synthesis of Ag nanostructures, and is thus broadly used for the chemical deposition of Ag coatings on various substrates and mass production of Ag particles.[26, 27] In particular, Ag is a highly conductive and superior electron transmitting material; therefore, it can allow for superior electron transfer in chemical and bio-sensors.[3, 28, 29] As previously reported, the typical experimental procedure using the Tollens' reaction for preparing Ag nanoparticles involves four steps: (i) preparing the silver and reducing solutions; (ii) mixing the two solutions homogeneously; (iii) pouring quickly onto the target substrate; and (iv) quenching the reaction using a 20× diluted ammonia solution after the desired growth time. The silver and reducing solutions were prepared accordingly to the typical protocol of the Tollens' reaction for Ag nanoparticle synthesis.[1] First, the silver solution was prepared by adding silver nitrate (1.7 g) to deionized water (20 mL) with potassium hydroxide (40 μL, 0.25 M). Ammonium hydroxide (28–32%) (~1.7 mL) was then added until the solution became clear and transparent again. Second, the

View Article Online
DOI: 10.1039/C7NR02354E

reducing solution was prepared by dissolving D-glucose (6.84 g) in deionized water (20 mL) and then adding absolute methanol (10 mL) to the obtained solution.

After drying the water-soaked PDMS device using nitrogen gas, oxygen plasma was applied onto the micro/nanopatterns side under 15 sccm of O_2 and 10 W for 10 s (Cute-MP, Femto Science, Hwaseong, Korea). This process rendered the surface of the PDMS device hydrophilic and simultaneously prevented permanent bonding of the device to the substrate. The prepared PDMS device was placed on a piece (2×3 cm^2 in size) of silicon dioxide (500 nm in thickness)/silicon wafer (SiO_2/Si wafer, LG Siltron, Gumi, Korea), and kept on a square dish with water-soaked paper for maintaining proper humidity.

Equations (1) – (3) represent the chemical processes occurring when the Tollens' reaction is involved in the synthesis of Ag nanoparticles. In these reactions, $AgNO_3$ plays a key role as the precursor of $Ag(NH_3)_2OH$, which is reduced by glucose or an aldehyde-containing compound for Ag nanoparticle generation.[1]

$$2AgNO_3 + 2NaOH \rightarrow Ag_2O_{(s)} + 2NaNO_3 + H_2O \quad (1)$$

$$Ag_2O_{(s)} + 4NH_3 + 2NaNO_3 + H_2O \rightarrow 2[Ag(NH_3)_2]NO_3 + 2NaOH \quad (2)$$

$$2[Ag(NH_3)_2]^+ + RCHO + H_2O \rightarrow 2Ag_{(s)} + 4NH_3 + RCO_2H + 2H^+ \quad (3)$$

2.5. Experimental setup and data analysis

To evaluate the structural properties of the synthesized AgNB arrays, atomic force microscopy (AFM, DI-3100, Veeco, New York, USA), field emission-scanning electron microscopy (FE-SEM, S-4800, Hitachi, Tokyo, Japan) and energy-dispersive spectroscopy (EDS, EMAX, Mahwah, USA) were conducted. For the electrical characterization in view of amperometric sensor applications, the AgNBs were connected to external bridge electrodes. The AgNBs synthesized on the SiO_2/Si substrates were 200 μm in length and the number of the individual AgNBs was controlled to be 5, 10, 20, 30, 40 and 50, respectively. Two electrodes were microfabricated on both sides of the AgNBs with a 100 μm spacing using a standard photolithography technology, that is, a negative photoresist (AZ5214) was patterned

View Article Online
DOI: 10.1039/C7NR02354E

using a photomask with 100 μm feature sizes, and then 50-nm-thick Ti and 250-nm-thick Au layers were sequentially deposited using an electron beam evaporator (WC-4000, Woosung Hi-vac, Korea). The electrode fabrication was completed after lift-off and the AgNB-integrated microdevice was ready for electrical measurements. The electrical properties of the AgNBs were measured using a source meter (2612A, Keithley, Cleveland, USA) and a custom-made data acquisition program (Labview, National Instruments, Austin, USA). Optical intensities were measured from optical images obtained by a CCD camera (ORCA R2, Hamamatsu, Japan) equipped with a microscope (Ti-U, Nikon, Japan) using an image processing software (Image J, NIH, USA). Optical intensities ranged from 0 (white) to 255 (black) in case of an 8-bit-black-and-white optical image as used in this work.

3. Results and Discussion

3.1. Fabrication of micro-/nanofluidic platforms using crack-photolithography

Figure 1 illustrates the cracking-assisted microfabrication process of a micro-/nanofluidic platform by standard photolithography, which yields features with a size of about 2–5 μm. The standard crack-photolithography process is described in detail in the Supporting Information (see Figure S1). The first step is to design a photomask for a microfluidic channel network, which is used for solution loading. However, notched (crack initiation) and round structures (crack termination) need to be added wherever crack nanopatterns (nanochannels) are required, without limitation in directionality and length (up to 1 mm) (Figure 1a).[22, 23] Figure 1b shows a fabricated SU-8 pattern, in which well-developed crack nanopatterns are formed on the micropattern surfaces. The 3D schematic illustration in Figure 1c helps us to visualize the hybrid-scale micro-/nanopatterns.

Typically, crack nanopatterns are generated in a nanoslit format, whose aspect ratio is approximately 1:12.5 (i.e., 147.6 nm deep and 1.9 μm wide), as shown in Figure 1d,e; this is defined as the reference value for the crack nanopatterns. However, since crack nanopatterns

View Article Online
DOI: 10.1039/C7NR02354E

are essential to the controllable synthesis of various NBs, we attempted to precisely manipulate the geometrical dimension of such nanopatterns. In our previous work, we have found that the cross-linking density of SU-8 films is the most important factor determining the aspect ratios of crack nanopatterns[30-32] and the cross-linking density can be modulated by varying the exposure dose and annealing temperature. For this reason, we experimentally varied the exposure dose and annealing temperature. When the cross-linking density of SU-8 films increased, the depth (from 300 nm to 75 nm), width (from 2.0 μm to 0.8 μm), and aspect ratio (from 1:5.6 to 1:12.5) of the crack nanopatterns decreased. From these characterization results, we determined the optimal annealing conditions to obtain the deepest crack nanopatterns: i.e., soft bake (95 °C for 3 min), 1st post-exposure baking (PEB) (75 °C for 3 min), and 2nd PEB (115 °C for 3 min). As a result, we produced crack nanopatterns that are 300 nm deep and 1.6 μm wide, showing an aspect ratio of 1:5.6 (Figure 1f). The depth is two times that of the reference crack nanopattern. Notably, we demonstrated that crack-photolithography can be used to fabricate nanopatterns with a wide range of geometrical dimensions as per the researcher's needs. However, further characterization of the relationship between the aspect ratio and the fabrication conditions is beyond the scope of this work.

Figure 1g illustrates the soft lithography process used to produce a positive polyurethane acrylate (PUA) replica mold, and a negative PDMS de-molding device in which the micro-/nanofluidic platform from the SU-8 mold is repeatedly produced with high throughput and replication reliability (< 6.7% reduction in depth and/or width from an SU-8 mold to a PDMS device).[22, 23]

3.2. Synthesis and characterization of the AgNB arrays

Figure 2 shows the fabrication of a AgNB array using a micro-/nanofluidic platform and the Tollens' reaction. $AgNO_3$ and its reducing solution were individually loaded (20 μl each) through the two microfluidic channels that are connected by 200-μm-long and 300-nm-deep crack nanochannels (Figure 2a(i)), as illustrated in Figure 2a. The nanochannels completely

View Article Online
DOI: 10.1039/C7NR02354E

suppressed convection flow between the two microchannels but allowed silver precursors and the reductant molecules (i.e., glucose) to diffuse to the opposite side;[22] the Ag nanoparticle synthesis mechanism is described above. The generated Ag nanoparticles adhered onto the nanochannel walls, and then, they grew further and were allowed to combine with the neighboring nanoparticles. Since the Ag nanoparticles were physically constrained within the nanochannel, they formed a NB with high porosity along the nanochannel. Figure 2a(ii) shows a microscopic image of AgNBs on a Si-wafer, which are well aligned with the nanochannels. Note that the AgNB synthesis was performed in a container with high humidity for 4 h at room temperature (24 ˚C), which minimized the evaporation of solutions in the nanochannels through PDMS. Then the PDMS device was gently detached from the substrate. The reaction was quenched by soaking the substrate in 20:1 H_2O:NH_4OH solution for 30 s and subsequently in deionized water.

Figure 2b shows a single AgNB, which was revealed to be pure silver, as desired, by energy dispersive spectroscopy analysis (see Figure S2 in the Supporting Information). The height and width of the AgNBs were fairly uniform, but the density gradually decreased from the left side to the right side of the nanochannels, showing strong dependence on the concentration of $AgNO_3$ and reducing agent. The surface morphology varied as well along the concentration gradient, and the resulting aspect ratios were about 1:11 (i.e., 200 nm high and 2.2 μm wide), as shown in Figure 2c. This can be attributed to the elastomeric nature of PDMS; the bonding and roof sagging of the PDMS device on the substrate may additionally decrease the aspect ratios. In addition, we demonstrated that a AgNB array can be easily produced in a high-throughput manner by using the same synthesis approach. Since 2,207 crack nanochannels were fabricated between a pair of microchannels on a 3 cm × 5 cm Si substrate, the same number of AgNBs were synthesized, as shown in Figure 2d (see Supporting Movie S1).

View Article Online
DOI: 10.1039/C7NR02354E

We further investigated the effect of reaction temperatures and Ag precursor concentrations on AgNB synthesis by directly observing the AgNB synthesis in a nanochannel; for this, the Si substrate was replaced with a transparent glass substrate. As shown in Figure 2e, AgNBs started to grow with time from the left side at low temperature (25 °C) and from the right side at high temperature (45 °C) (see Supporting Movies S2 and S3). This result can be explained by the energy diagram and growth model. Basically, a reduction potential of 0.373 V is required to reduce $Ag(NH_3)^+$ to Ag(s) and this potential is significantly affected by several factors such as pH, concentration, and reaction temperature.[27, 33, 34] Among these factors, the reductant concentration can enhance the catalytic activity when it increases; hence, it appears that Ag nanoparticles are first generated on the left side, where the concentration of reducing molecules is higher.[35] On the other hand, at high temperature, the reduction potential is already high, and hence, Ag nanoparticles are generated as soon as the reducing molecules are exposed to the Ag precursors in the nanochannel. Since the diffusivity of the reducing agent (i.e., $D_g = 6.75 \times 10^6$ cm^2/s at 25 °C) is much higher than that of $AgNO_3$ ($D_A = 0.6 \times 10^6$ cm^2/s at 25 °C) in water,[36, 37] glucose molecules diffuse from the left to the right side of the nanochannel almost 11.3 times faster than the opposite case involving $AgNO_3$ precursors (arriving time ratio = $t_g/t_A \sim D_A/D_g \sim 11.3$). Therefore, Ag nanoparticles are generated from the right side of the nanochannel. Figure S3 in the Supporting Information shows the relative optical intensities of the AgNB in grey scale across the nanochannel around the center of the nanochannel over 800 min when the temperature was varied from 15 °C to 45 °C at 10 °C intervals. The relative intensities linearly increased and then leveled off at similar values, with no distinct difference at 15 °C until 700 min. This trend can be attributed to the insufficient reduction potential, as described above (Figure S3b). Figure S4 shows the morphological differences caused only by a different reaction temperature, all other synthesis conditions being the same. It can be seen that the AgNB

synthesized at a higher temperature (25 °C) is composed of bigger Ag nanoparticles with higher porosity than that synthesized at a lower temperature (20 °C).

Next, we measured the relative optical intensities of the AgNB synthesized at three different concentrations of $AgNO_3$ (0.1 M, 0.5 M, and 1 M) at three different positions along a nanochannel as a function of the reaction time (Figure S3c). Under all the tested concentrations, AgNBs were generated from the left side of the nanochannel, but a high concentration (1 M) of $AgNO_3$ induced an earlier synthesis of the AgNW as compared to that lower concentrations (0.1 and 0.5 M). This can be attributed to the increased possibility of a reduction reaction at a higher concentration of the reductant. As a result, a high concentration of $AgNO_3$ resulted in higher growth rates and higher relative saturating intensities compared to those at lower concentrations. Thus, AgNB synthesis can be controlled by manipulating the reaction temperature and concentration of the precursor solution. Moreover, the reaction can be stopped by perfusing the microchannels with a fresh solution of water, implying that the reaction time can also be actively controlled. We successfully demonstrated that the cracking-assisted micro-/nanofluidic platform alongside the Tollens' reaction can provide a novel method for fabricating AgNWs on a chip.

3.3. Nanosensor application of the AgNB array for H_2O_2 detection

Figure 3a shows a AgNB-integrated microdevice that was fabricated by additionally depositing Ti/Au electrodes via conventional photolithography and by using an electron beam evaporator. Micropatterns for the two electrodes were produced by manually aligning a chrome mask at the center of the AgNB, followed by sequential deposition of 50 nm thick Ti and 250 nm thick Au, and a final lift-off process. Consequently, the Ti/Au electrodes were micropatterned over the 200-μm-long AgNB array with 100 μm spacing distance; more details of the process are described in the Experimental section. Figure 3b shows a characteristic current (I)-voltage (V) curve of the microdevices with different numbers of AgNBs. In other words, 5, 10, 20, 30, 40, and 50 AgNBs were tested from 0.2 V to 0.5 V and

View Article Online
DOI: 10.1039/C7NR02354E

the resistances were measured to be 135.1, 50.8, 46.9, 36.6, 18.8, and 14.0 kΩ, respectively. The explanation for this result seems to be straightforward because the increase in the number of AgNBs causes a gradual decrease in the parallel resistance. As demonstrated in Figure 2, the number of AgNBs can be easily controlled by crack-photolithography, thereby implying that a AgNB-integrated microdevice can provide a wide range of I-V characteristic curves, which play an important role in chemical sensors. The as-prepared AgNBs were used to detect H_2O_2 solution on the basis of their amperometric response; this was feasible because of the excellent catalytic activity of Ag.[38]

Figure 3c shows the typical amperometric responses of the AgNB-integrated microdevice (50 AgNBs) when 10 μl H_2O_2 droplets were dropped on top of the AgNB array at a fixed potential of 0.4 V. Six different concentrations were sequentially tested, and the current was found to increase with the concentration. Each measurement was conducted for 10 min. Before subsequent measurements, the microdevice was properly cleaned using deionized water for 1 min, and subsequently dried under nitrogen. The detection mechanism can be explained by the following electrochemical reactions:[39]

$$O_2 \text{ (dissolved)} \rightarrow O_2 \text{ (adsorbed)} \quad (4)$$

$$O_2 \text{ (adsorbed)} + e^- \rightarrow O_2^- \text{ (adsorbed)} \quad (5)$$

$$2H_2O_2 + O_2^- \rightarrow 2H_2O + 2O_2 + e^- \quad (6)$$

Essentially, dioxygen (O_2) molecules are chemisorbed onto the surface of the AgNBs so that O_2^- is generated under the positive bias. Subsequently, O_2^- protonates H_2O_2 to H_2O, releasing a free electron, thereby increasing the electric current through the AgNBs. The measured current density increases with an increase in the concentration of H_2O_2. This can also be explained using the same oxidation mechanism above and Michaelis-Menten-type kinetics.[40] As a result, the oxidation current gradually increases with increasing H_2O_2 concentration.

Figure 3d shows the curve-fitting result for the plot of the logarithmic concentrations (C) of H_2O_2 and the measured currents. An almost linear plot, I (μA) = 1.60 log (C) + 24.03, with

View Article Online
DOI: 10.1039/C7NR02354E

a correlation coefficient of R = 0.9750 was observed. The detection limit (DL) of the microdevice was approximately 84.3 nM, as calculated using the equation DL = K × Sb_1/S, where the coverage factor is K = 3 (R = 0.9750), Sb_1 is the standard deviation of the blank solution (DI water), and S is the slope of the calibration curve.[41] The DLs of other Ag-nanostructure-based H_2O_2 sensors are summarized in Table S1 in the Supporting Information. The performance of our microdevice was better than that of devices based on other Ag-nanostructure-based electrodes and comparable to that of devices based on enzyme-modified electrodes. This result could be attributed to the high surface area of the AgNWs.[3, 38, 42] Notably, our AgNBs were fabricated from Ag nanoparticles in the nanochannel and hence showed a higher porosity than those of conventionally fabricated flat NBs. Further, mass production of our microdevice can be achieved at reduced cost and labor, providing a much simpler means to obtain high chemical sensing performance without device degradation that is caused by enzyme denaturation.[43] We note that our AgNB-integrated microdevice can be fabricated using only microfabrication technologies without the need for expensive nanofabrication equipment or tools.

3.4. A microfluidic device integrated with a AgNB array for H_2O_2 detection

Figure 4 shows that our method can be applied to the development of a NB-embedded microfluidic device. Figure 4a illustrates the NW transfer from a silicon wafer to a PDMS device. First, 50 NBs were synthesized by using the same number of crack nanochannels, and then, they were transferred onto the PDMS device via a detachment process. In particular, we intended to continue the Ag NB synthesis for 24 h for the complete formation of Ag nanoparticles in the nanochannel. The Ag nanoparticles were in turn converted into AgNWs, which were transferred onto the PDMS device during the detachment process. In other words, when the reaction was carried out for a sufficient time, the nanochannel appeared very dark, implying that it was completely filled with Ag nanoparticles and/or AgNBs, which facilitated the detachment process. Additional Ti/Au electrodes were fabricated in the same manner as

View Article Online
DOI: 10.1039/C7NR02354E

described before. Notably, the electrode patterning process using a shadow mask, which has a feature size of 100 μm, could minimize unnecessary stress on the flexible PDMS substrate because no additional lift-off process was required. The top PDMS device with a microfluidic channel that allows fluid flow to the NBs was easily bonded to another PDMS device using O_2 plasma treatment.

Figure 4b shows the fabricated PDMS device in which the transferred AgNBs and deposited Ti/Au electrodes are integrated with the microfluidic channel network. Figure 4c shows the I-V curve, which exhibits good Ohmic behavior, and two insets: an optical image (white) and an SEM image (blue) of the transferred AgNB. The PDMS-embedded AgNB array showed 2.5-fold higher resistance (34.7 kΩ) than that observed for the same number of AgNBs on a SiO_2/Si substrate (14.0 kΩ). This difference can be explained as follows. As the contact resistance between metal electrodes, which were used for electrically connecting AgNBs and made of Ti/Au, and measuring probes can be affected by the soft and flexible PDMS substrate. In other words, the surfaces of the metal electrodes on the PDMS substrate can be easily damaged, partially broken during the fabrication process. In addition, the electrical measurement can be affected because of poor mechanical contact with measuring probes. If the surfaces are electrically disconnected or the contact areas are not sufficient, the contact resistance can be dramatically increased. As a result, the conductivity of the PDMS-embedded AgNBs can be measured to be low. For these reasons, the PDMS-embedded AgNBs can have a higher resistance than AgNBs on a SiO_2 substrate. Similarly, a 1.3 mM H_2O_2 solution was introduced into the microfluidic device and it was guided along the microfluidic channel directly to the AgNB array. Figure 4d shows the current measurement under 0.4 V, indicating a dramatic increase in the current in 20 s. The slightly retarded response time can be attributed to a continuously changing non-equilibrium depletion layer and associated relaxation effects near the electrode in the microfluidic channel.[44] However, we evidently demonstrated that the AgNB array can be easily embedded in various PDMS

View Article Online
DOI: 10.1039/C7NR02354E

microfluidic devices. Therefore, our NB synthesis and transfer method can open a novel route for a variety of NB-integrated microfluidic bio-/chemical sensor applications. Since the AgNB synthesis and integration do not require a high-temperature reaction, the strategy could be widely applied to various substrates for AgNB-integrated, flexible microsystems.

So far, we have demonstrated not only an unconventional technique for the fabrication of a micro-/nanofluidic channel network using crack-photolithography, but also a novel NB synthesis technique that combines the micro-/nanofluidic channel network and Tollens' reaction. First, it is worthwhile discussing the feature size of the synthesized AgNBs, which are larger than about 100 nm in height and 1 μm in width. The shapes of the NBs were constrained by the nanofluidic channel, so that the feature size could be well controlled by manipulating the dimension and geometry of the cracks. Second, the NB synthesis is based on the mass transport of metallic precursors and reducing agents in opposite directions, so that the uniformity of the NBs depends on their local concentrations. This can be a disadvantage of the proposed fabrication platform, but the synthesized NWs can be more uniform and well connected if the reaction temperature is decreased or if an additional thermal annealing process is introduced; for low temperature processes, NW synthesis takes longer. However, it is noted that the fabrication platform can produce NBs with even higher porosity compared to NBs fabricated by other methods. Third, the fabrication platform shows a unique advantage with regard to fabrication throughput, time, and cost. Since an SU-8 mold can be used for several PUA replications and each PUA mold can be re-used for several tens of PDMS replications, one micro-/nanofluidic channel network can produce several hundreds of PDMS devices with high repeatability. Therefore, the NB fabrication platform makes it possible to produce NWs in a repeatable, high-throughput, and low-cost manner. Fourth, the fabrication platform allows the simultaneous synthesis and alignment of NBs on a chip, eliminating the need for special micro-/nanofabrication equipment and dramatically reducing the consumption of time, labor, and cost. Fifth, the applicability of the fabrication platform can be

View Article Online
DOI: 10.1039/C7NR02354E

extended to various other aqueous solutions containing metallic species such as ZnO, SiO_2, Au, and Cu.[45-49] In conjunction with reducing solutions, the fabrication platform could be used for the synthesis of not only other metallic NBs in a similar fashion but also multiple metallic NBs on a chip by designing a micro-/nanofluidic channel network via other strategies.

4. Conclusions

In conclusion, we successfully demonstrated a novel NB fabrication technique using a crack-photolithography-based micro-/nanofluidic platform and a solution-based chemical synthesis, wherein conditions that allowed diffusion and prevented convection facilitated reaction between the Ag precursors and the reducing agents to generate Ag nanoparticles. We applied the crack-photolithography process to precisely manipulate the geometrical dimensions of the cracks (with aspect ratios ranging from 1:10 to 1:6) by modulating the mechanical properties of the SU-8 film. Using the replicated crack nanochannels, various AgNBs were synthesized solely by standard photolithography, and more than 2,200 AgNBs were fabricated in a well-aligned and high-throughput manner on a chip. Additionally, we demonstrated that the synthesized AgNBs work as a H_2O_2 sensor with performance better than or comparable to that of other silver-nanostructure-based chemical sensor devices. Furthermore, we demonstrated that AgNBs synthesized on a SiO_2/Si substrate are easily transferred to other substrates such as PDMS, indicating tremendous potential for integrating the NBs into conventional microfluidic devices. In future, this technique might be useful for the integration of NBs fabricated from multiple materials into a single microsystem for a wide range of bio- and chemical nanosensor applications.

Supporting Information

Supporting Information is available from the web site.

Acknowledgements

This work was supported by the National Research Foundation of Korea (NRF) grant funded by the Korean government (MSIP) (NRF-2014R1A2A1A10050431).

References

1. B. Sciacca, J. van de Groep, A. Polman and E. C. Garnett, *Adv. Mater.*, 2016, **28**, 905-909.
2. M. A. Zimmler, D. Stichtenoth, C. Ronning, W. Yi, V. Narayanamurti, T. Voss and F. Capasso, *Nano Lett.*, 2008, **8**, 1695-1699.
3. M.-J. Song, S. W. Hwang and D. Whang, *J. Appl. Electrochem.*, 2010, **40**, 2099-2105.
4. X. Chen, C. K. Wong, C. A. Yuan and G. Zhang, *Sensor Actuat. B-Chem.*, 2013, **177**, 178-195.
5. Y. Wu and P. Yang, *J. Am. Chem. Soc.*, 2001, **123**, 3165-3166.
6. Z. Miao, D. Xu, J. Ouyang, G. Guo, X. Zhao and Y. Tang, *Nano Lette.*, 2002, **2**, 717-720.
7. Z. Huang, N. Geyer, P. Werner, J. De Boor and U. Gösele, *Adv. Mater.*, 2011, **23**, 285-308.
8. K. Lee, T. Choi, S. Lee and D. Poulikakos, *Nanotechnology*, 2010, **21**, 125301.
9. S. Raychaudhuri, S. A. Dayeh, D. Wang and E. T. Yu, *Nano Lett.*, 2009, **9**, 2260-2266.
10. A. R. Tao, J. Huang and P. Yang, *Accounts Chem. Res.*, 2008, **41**, 1662-1673.
11. M. Law, J. Goldberger and P. Yang, *Annu. Rev. Mater. Res.*, 2004, **34**, 83-122.
12. L. Bischoff, B. Schmidt, H. Lange and D. Donzev, *Nucl. Instrum. Meth. B*, 2009, **267**, 1372-1375.
13. M. Austin and S. Y. Chou, *J. Vac. Sci. Technol. B*, 2002, **20**, 665-667.
14. M. Schvartzman, D. Tsivion, D. Mahalu, O. Raslin and E. Joselevich, *P. Natl. Acad. Sci. USA*, 2013, **110**, 15195-15200.
15. D. Gedamu, O. Lupan, Y. K. Mishra and R. Adelung, *J. Nanoelectron. Optoelectron.*, 2014, **9**, 239-246.
16. M. Kim, D.-J. Kim, D. Ha and T. Kim, *Nanoscale*, 2016, **8**, 9461-9479.
17. N. M. Doan, L. Qiang, Z. Li, S. Vaddiraju, G. W. Bishop, J. F. Rusling and F. Papadimitrakopoulos, *Sensors*, 2015, **15**, 6091-6104.
18. V. Abramova, A. S. Slesarev and J. M. Tour, *Nano Lett.*, 2015, **15**, 2933-2937.
19. V. Abramova, R. Adelung, O. C. Aktas, J. Franc, A. Biswas, R. Kunz, M. Elbahri, J. Kanzow, U. Schürmann and F. Faupel, *Nat Mater.*, 2004, **3**, 375-379.
20. S. Jebril, M. Elbahri, G. Titazu, K. Subannajui, S. Essa, F. Niebelschütz, C. C. Röhlig, V. Cimalla, O. Ambacher and B. Schmidt, *Small*, 2008, **4**, 2214-2221.
21. T. W. Odom, J. C. Love, D. B. Wolfe, K. E. Paul and G. M. Whitesides, *Langmuir*, 2002, **18**, 5314-5320.
22. M. Kim and T. Kim, *Anal. Chem.*, 2015, **87**, 11215-11223.
23. M. Kim, D. Ha and T. Kim, *Nat. Commun.*, 2015, **6**, 6247.
24. M. Jamal, A. M. Zarafshar and D. H. Gracias, *Nat. Commun.*, 2011, 2, 527.
25. J. B. Boreyko, P. Mruetusatorn, S. T. Retterer and C. P. Collier, *Lab Chip*, 2013, **13**, 1295-1301.
26. M. Rycenga, C. M. Cobley, J. Zeng, W. Li, C. H. Moran, Q. Zhang, D. Qin and Y. Xia, *Chem. Rev.*, 2011, **111**, 3669-3712.
27. J. I. Hussain, A. Talib, S. Kumar, S. A. AL-Thabaiti, A. A. Hashmi and Z. Khan, *Colloid Surface A*, 2011, **381**, 23-30.
28. J. van de Groep, D. Gupta, M. A. Verschuuren, M. M. Wienk, R. A. Janssen and A. Polman, *Sci. Rep.*, 2015, **5**, 11414.
29. C. Ren, Y. Song, Z. Li and G. Zhu, *Anal. Bioanal. Chem.*, 2005, **381**, 1179-1185.
30. T. A. Anhoj, A. M. Jorgensen, D. A. Zauner and J. Hübner, *J. Micromech. Microeng.*, 2006, **16**, 1819.
31. J. D. Williams and W. Wang, *J. Microlith. Microfab.*, 2004, **3**, 563-568.

32. D. Sameoto, S. Tsang, I. Foulds, S. Lee and M. Parameswaran, *J. Micromech. Microeng.*, 2007, **17**, 1093-1098.
33. M. Smith and M. Pierson, *Appl. Environ. Microb.*, 1979, **37**, 978-984.
34. C. DIJK and C. VEEGER, *Eur. J. Biochem.*, 1981, **114**, 209-219.
35. M. Kumari, A. Mishra, S. Pandey, S. P. Singh, V. Chaudhry, M. K. R. Mudiam, S. Shukla, P. Kakkar and C. S. Nautiyal, *Sci. Rep.*, 2016, **6**, 27575.
36. H. Uedaira and H. Uedaira, *J. Solution Chem.*, 1985, **14**, 27-34.
37. G. Janz, G. Lakshminarayanan, M. Klotzkin and G. Mayer, *J. Phys. Chem.*, 1966, **70**, 536-539.
38. X. Qin, H. Wang, X. Wang, Z. Miao, Y. Fang, Q. Chen and X. Shao, *Electrochim. Acta*, 2011, **56**, 3170-3174.
39. N. H. Al-Hardan, M. A. Abdul Hamid, R. Shamsudin, N. K. Othman and L. Kar Keng, *Sensors*, 2016, **16**, 1004.
40. S. B. Hall, E. A. Khudaish and A. L. Hart, *Electrochim. Acta*, 1998, **43**, 579-588.
41. A. Barba-Bon, A. M. Costero, S. Gil, M. Parra, J. Soto, R. Martínez-Máñez and F. Sancenón, *Chem. Commun.*, 2012, **48**, 3000-3002.
42. B. Zhao, Z. Liu, Z. Liu, G. Liu, Z. Li, J. Wang and X. Dong, *Electrochem. Commun.*, 2009, **11**, 1707-1710.
43. L. Zhang, Z. Fang, Y. Ni and G. Zhao, *Int. J. Electrochem. Soc*, 2009, 4, 407-413.
44. R. Trouillon and M. A. Gijs, *Lab Chip*, 2014, **14**, 2929-2940.
45. M. Guerrero, J. Zhang, A. Altube, E. García-Lecina, M. Roldan, M. D. Baró, E. Pellicer and J. Sort, *Sci. Technol. Adv. Mat.*, 2016, **17**, 177-187.
46. A. Kuijk, A. van Blaaderen and A. Imhof, *J Am Chem Soc*, 2011, 133, 2346-2349.
47. J. Polte, R. Erler, A. F. Thunemann, S. Sokolov, T. T. Ahner, K. Rademann, F. Emmerling and R. Kraehnert, *Acs Nano*, 2010, **4**, 1076-1082.
48. J. Wagner, T. Tshikhudo and J. Köhler, *Chem. Eng. J.*, 2008, **135**, S104-S109.
49. W. Hong, J. Wang and E. Wang, *Nanoscale*, 2016, **8**, 4927-4932.

Figures

View Article Online
DOI: 10.1039/C7NR02354E

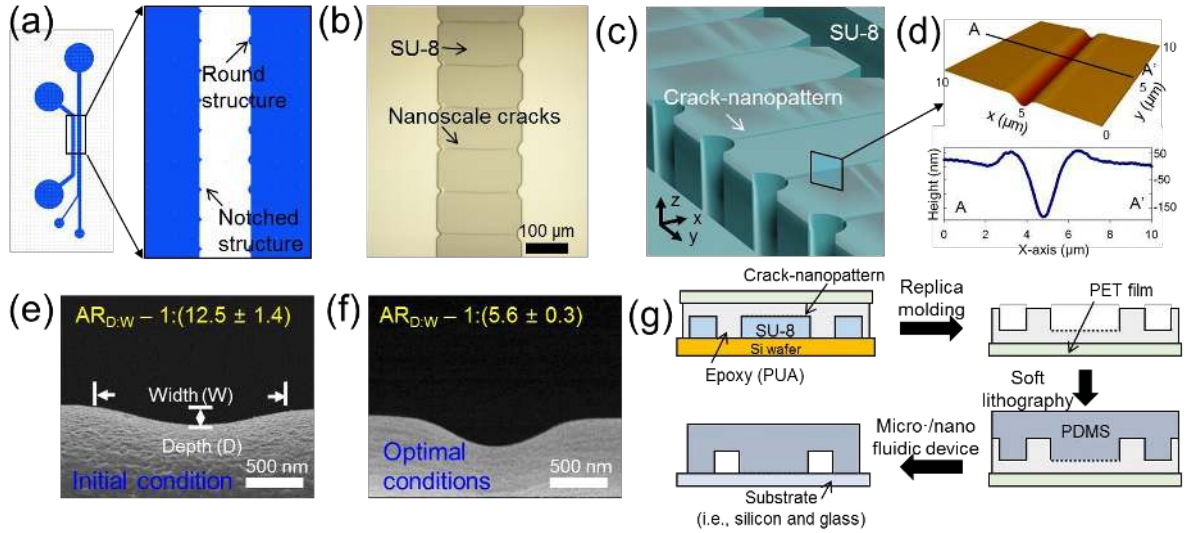

Figure 1. Cracking-assisted micro-/nanofluidic channel network. (a) Mask design for crack-photolithography. Microchannels with notched and round structures for crack-based nanochannels. (b) Microscopic image of an SU-8 mold with nanoscale cracks that are initiated at the notch points and terminated at the round structures. (c) 3D schematic showing crack nanopatterns on the SU-8 film. (d) AFM image of a crack nanopattern and the cross-cut along A–A'. (e,f) Cross-sectional FE-SEM images of crack nanopatterns on the SU-8 film, the aspect ratios of which are modulated by the fabrication process: previous and optimal (this work) conditions. (g) Fabrication of micro-/nanofluidic platform by using PUA replication and soft lithography.

View Article Online
DOI: 10.1039/C7NR02354E

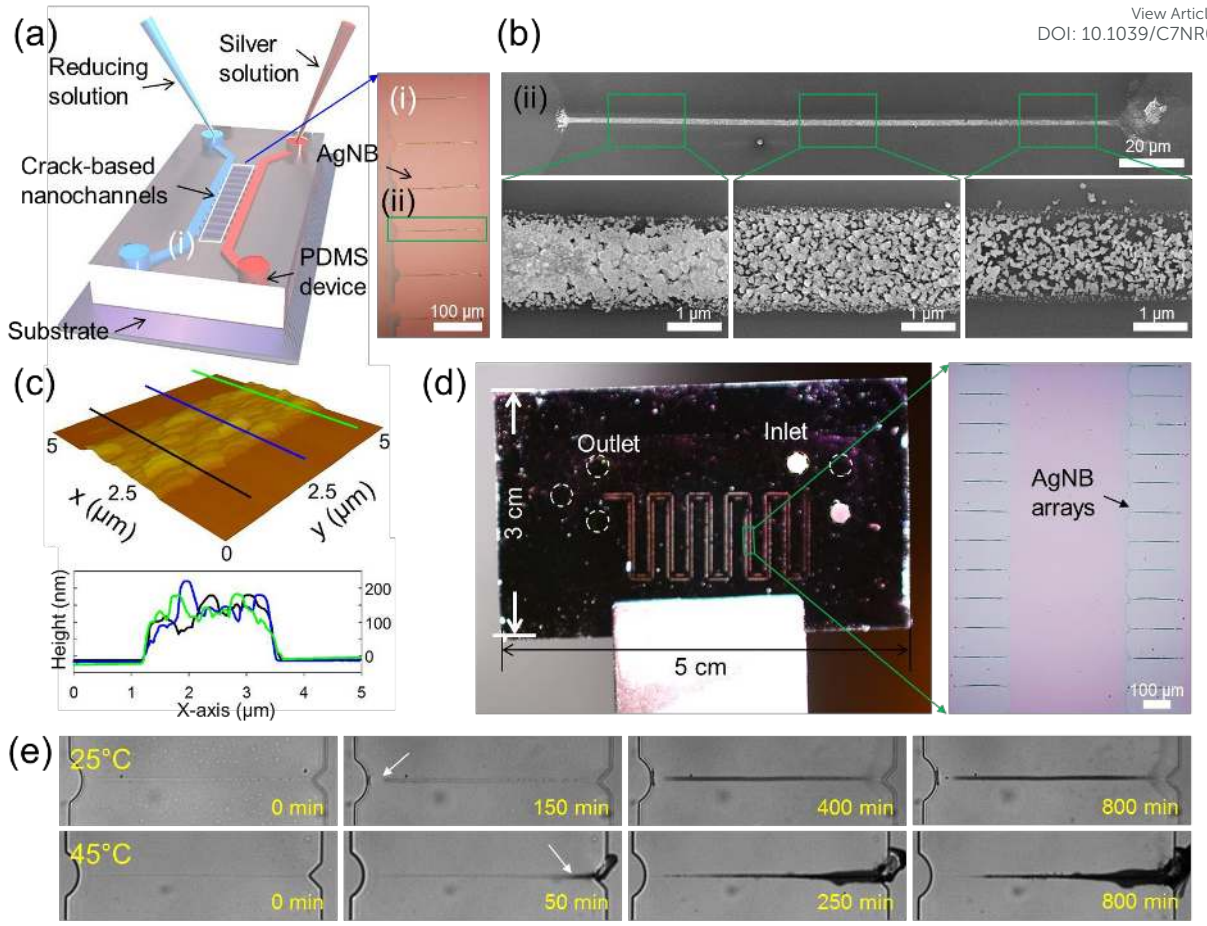

Figure 2. Fabrication of AgNBs using a micro-/nanofluidic platform and the Tollens' reaction. (a) Schematic illustration showing a NW fabrication platform in which silver and its reducing solution are allowed to flow along the microchannels (i) and AgNBs are synthesized in the nanochannels (ii) via mass transport and chemical reaction. The microscopic image shows a synthesized AgNB array. (b) FE-SEM images of a single AgNB and its enlarged images at three different locations. (c) AFM image of the AgNB and the cross-cuts along the lines (black, blue, and green), respectively. (d) Photographic image of fabricated AgNWs that were synthesized by using 2,207 nanochannels along a long microchannel. The enlarged microscopic images show a part of the AgNB array. (e) Time-lapse microscopic images of the AgNB synthesis process over 800 min at two different temperatures (25 °C and 45 °C).

View Article Online
DOI: 10.1039/C7NR02354E

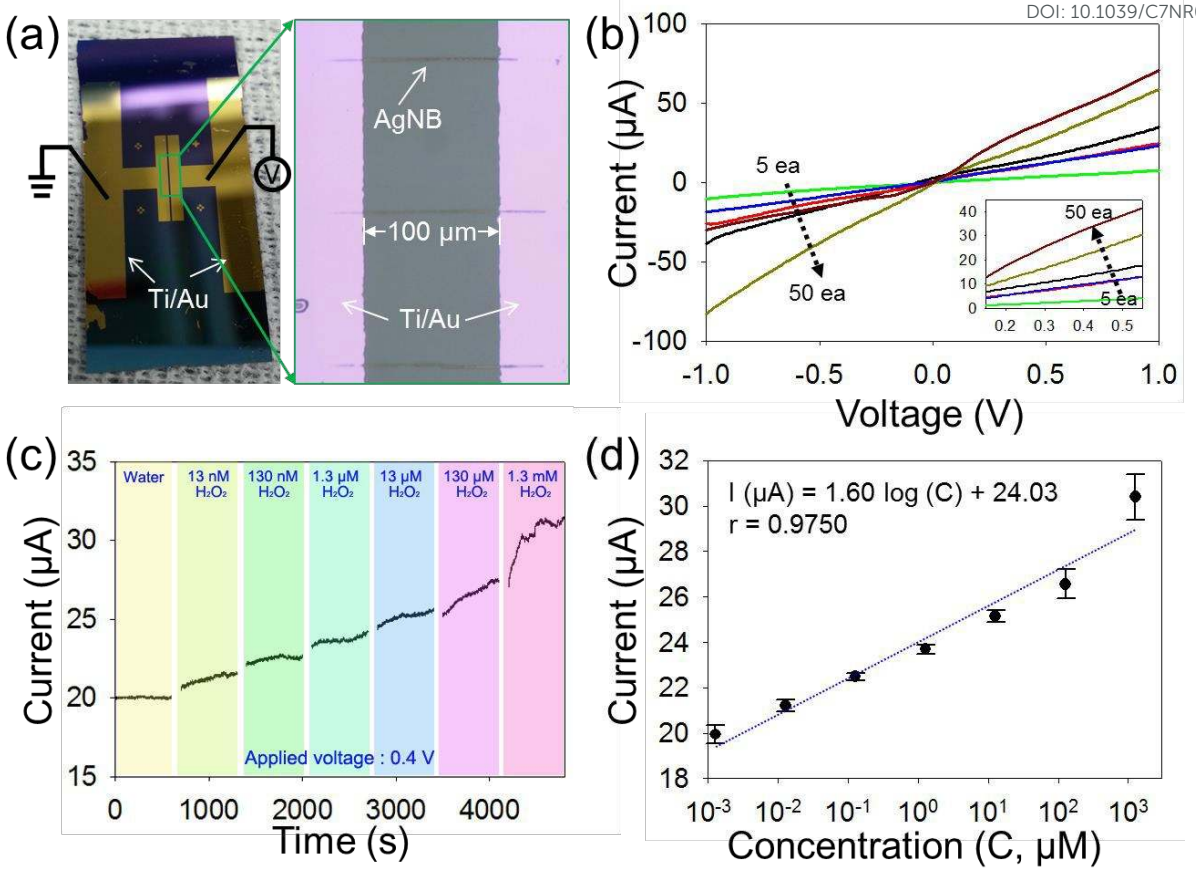

Figure 3. Characterization of a AgNB array device for electrochemical sensing of H_2O_2. (a) Photographic image of a AgNB array device integrated with Ti/Au electrodes (50/250 nm thickness). The enlarged microscopic image shows AgNBs between the two electrodes. (b) I-V curves of the AgNB device with different numbers of AgNBs (5, 10, 20, 30, 40, and 50). The inset shows the enlarged I-V curves from 0.15 to 0.55 V. (c) The amperometric responses of the AgNB device in the presence of H_2O_2 solution with six different concentrations at an applied potential of 0.4 V. (d) Curve-fitting result of the average currents and concentrations of H_2O_2.

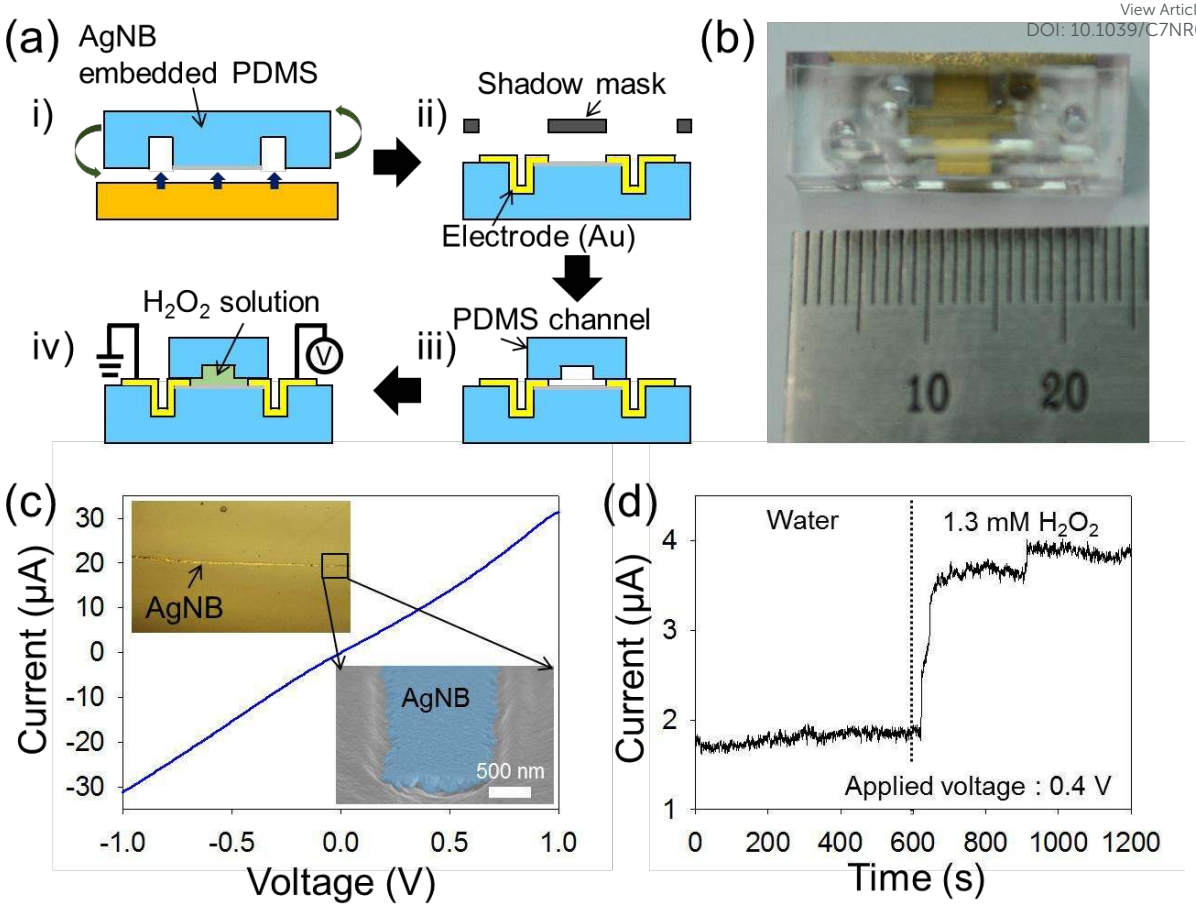

Figure 4. Integration of a AgNB array into a flexible microfluidic device and its application to a H_2O_2 sensor. (a) Fabrication process of a AgNB embedded microfluidic device: i) transfer of AgNBs from a Si substrate (detachment) to a PDMS device (attachment), ii) deposition of Au electrodes through a shadow mask, iii) bonding of a PDMS slab with microchannels for H_2O_2 loading, and iv) electrical measurement from the electrodes on flowing H_2O_2 solution. (b) Photographic image of the AgNB embedded microfluidic device. (c) I-V curve obtained from the device with 50 AgNBs. The inset represents an optical microscopic (left) and SEM (right) image of a AgNB transferred onto the PDMS. (d) Amperometric response of the AgNB-embedded microfluidic device at 0.4 V under 1.3 mM H_2O_2 flow.